

Global Mapping of the Surface Composition on an Exo-Earth using Color Variability

HAJIME KAWAHARA ^{1,2}

¹*Department of Earth and Planetary Science, The University of Tokyo, 7-3-1, Hongo, Tokyo, Japan*

²*Research Center for the Early Universe, School of Science, The University of Tokyo, Tokyo 113-0033, Japan*

(Received 2020 March 1; Revised 2020 April 3; Accepted 2020 April 6)

ABSTRACT

Photometric variation of a directly imaged planet contains information on both the geography and spectra of the planetary surface. We propose a novel technique that disentangles the spatial and spectral information from the multi-band reflected light curve. This will enable us to compose a two-dimensional map of the surface composition of a planet with no prior assumption on the individual spectra, except for the number of independent surface components. We solve the unified inverse problem of the spin-orbit tomography and spectral unmixing by generalizing the non-negative matrix factorization (NMF) using a simplex volume minimization method. We evaluated our method on a toy cloudless Earth and observed that the new method could accurately retrieve the geography and unmix spectral components. Furthermore, our method is also applied to the real-color variability of the Earth as observed by Deep Space Climate Observatory (DSCOVR). The retrieved map explicitly depicts the actual geography of the Earth and unmixed spectra capture features of the ocean, continents, and clouds. It should be noted that, the two unmixed spectra consisting of the reproduced continents resemble those of soil and vegetation.

Keywords: astrobiology – Earth – scattering – techniques: photometric, nonnegative matrix factorization

1. INTRODUCTION

Direct imaging of terrestrial planets around a nearby solar-type star are important targets in future astronomy. In the 2020 decadal surveys, both *HabEx* and *LUVOR* have shown a capability to search for these planets, even in the habitable zone. Direct imaging with spectroscopy provides information regarding the molecules in the atmosphere of the planet, which enables us to search for biosignatures such as oxygen, carbon dioxide, and water. Moreover, surface inhomogeneity can be explored with photometric monitoring of the reflected light as proposed by Ford et al. (2001). The color variability of the reflected light has been studied as a probe of surface compositions (e.g. Cowan et al.

2009; Fujii et al. 2011). The spatial distribution of the planet surface can also be inferred from the photometric variation. Diurnal variation, due to the rotation of the planet, provides the spin rotation period and a one-dimensional distribution of the surface (Pallé et al. 2008; Cowan et al. 2009; Oakley & Cash 2009; Fujii et al. 2010, 2011; Lustig-Yaeger et al. 2018). Furthermore, the axial tilt can be obtained from the analysis of the frequency modulation of the periodicity (Kawahara 2016; Nakagawa et al. 2020). The analytic expression of the reflected light curves has been studied (Cowan et al. 2013; Haggard & Cowan 2018).

A full two-dimensional inversion technique called “spin-orbit tomography” (analogous to computer tomography), was proposed by Kawahara & Fujii (2010), and has been studied in terms of the inverse problem (Kawahara & Fujii 2011; Fujii & Kawahara 2012; Farr et al. 2018; Berdyugina & Kuhn 2019; Aizawa et al. 2020) and obliquity measurement (Schwartz et al. 2016;

Farr et al. 2018). Recently, Luger et al. (2019) analyzed a single-band light curve of the Earth with Transiting Exoplanet Survey Satellite (TESS) data and inferred a rough two-dimensional cloud distribution. Fan et al. (2019) successfully retrieved a global map that was analogous to the distribution of a continent, from data that was obtained by DSCOVR by monitoring the Earth for two years (Jiang et al. 2018). They used the second principle component (PC2) of a multi-color light curve. Aizawa et al. (2020) improved the retrieved map from DSCOVR using sparse modeling. These examples showed that a global map could be retrieved from a time-series of a single band or PC. However, there exists a level of ambiguity when interpreting the derived maps when we do not have prior knowledge on the surface compositions.

Moreover, a blind retrieval of the reflectance spectra of the surface components from the integrated light is known as “spectral unmixing” in remote sensing. Cowan & Strait (2013) formulated the spectral unmixing as a disentanglement of geography by spin rotation. However, the longitudinal map inferred from the EPOXI data did not match with the real geographies because of the degeneracy of the inferred geometric distribution and spectral components (Fujii et al. 2017). The ambiguity of spectral unmixing originates from the matrix factorization not being unique, which has been extensively studied in the field of remote sensing. These studies found that additional constraints such as the simplex volume minimization of spectral components guarantee a unique solution to the unmixed spectra (Craig 1994; Fu et al. 2015; Lin et al. 2015; Fu et al. 2019; Ang & Gillis 2019). In practice, non-negative matrix factorization (NMF) with regularization terms easily retrieve the surface components in hyperspectral unmixing (Ang & Gillis 2019). These techniques in remote sensing are worth considering in their application to multi-color light curves of directly imaged exoplanets.

This paper aims to formulate a single inverse problem that unifies the spin-orbit tomography and spectral unmixing using a novel technique used in remote sensing. To achieve this, we unify the NMF-based spectral unmixing technique and spin-orbit tomography to retrieve both the spectra and geographies of a disk-integrated light curve from an exoplanet. We demonstrate its capabilities using the simulated data and real data from Deep Space Climate Observatory (DSCOVR). The rest of the paper is organized as follows. In Section 2, we first review the spin-orbit tomography and spectral unmixing. Next, we construct a unified retrieval model using NMF; the optimization scheme is also provided. In Section 3, we test the technique by applying it to a

cloudless toy model. In Section 4, we demonstrate this new technique by applying it to real observational data of the Earth recorded by DSCOVR. Finally, in Section 5, we summarize our results.

2. FORMULATION OF SPIN-ORBIT TOMOGRAPHY WITH SPECTRAL UNMIXING

2.1. Spin-Orbit Tomography

Space direct imaging in optical and near-infrared bands aim to detect reflected lights (or scattered lights) of a host star near a planet. The reflected light is a summation of photons from a day and visible side of a planet. This integrated-reflected light is expressed as

$$f_p = \frac{f_\star R_p^2}{\pi a^2} \int_{\text{IV}} d\Omega_1 R^s(\vartheta_0, \vartheta_1, \varphi) \cos \vartheta_0 \cos \vartheta_1, \quad (1)$$

where f_\star is the stellar flux, R_p is the radius of the planet, a is the star-planet distance, IV is the illuminated and visible area, and Ω_1 is the solid angle of the planets sphere. $R^s(\vartheta_0, \vartheta_1, \varphi)$ represents the bidirectional reflectance distribution function (BRDF) of the surface element s . ϑ_0 is the solar zenith angle, ϑ_1 is the zenith angle between the direction towards an observer and normal vector of the surface, and φ is the relative azimuth angle between the line-of-sight and stellar direction. The derivation of equation (1) is given in Appendix A. An isotropic approximation of the surface reflectance (the Lambert approximation), $R^s(\vartheta_0, \vartheta_1, \varphi) = R^s$, significantly reduces the complexity of the problem. We also define the spherical coordinate fixed on the surface by (θ, ϕ) and express the surface component s , in spherical coordinates $R^s = m(\theta, \phi)$ as the time-independent quantity (static surface approximation). Then, we obtain

$$f_p = \frac{f_\star R_p^2}{\pi a^2} \int_{\text{IV}} d\Omega_1 m(\theta, \phi) \cos \vartheta_0 \cos \vartheta_1. \quad (2)$$

We note that the IV area, $\cos \vartheta_0$, and $\cos \vartheta_1$ are time-dependent. The terms of $\cos \vartheta_0$ and $\cos \vartheta_1$ also depend on the position of the planet surface, (θ, ϕ) , and the axial tilt parameters, $\mathbf{g} = (\zeta, \Theta_{\text{eq}})$, where ζ is the planet obliquity and Θ_{eq} is the orbital phase at the equinox. We define the geometric kernel introduced by Kawahara & Fujii (2010) as

$$W_{\mathbf{g}}(t, \theta, \phi) = \begin{cases} \frac{f_\star R_p^2}{\pi a^2} \cos \vartheta_0 \cos \vartheta_1 & \text{for } \cos \vartheta_0, \cos \vartheta_1 > 0 \\ 0 & \text{otherwise,} \end{cases} \quad (3)$$

where the positive condition of $\cos \vartheta_0$ and $\cos \vartheta_1$ restrict the surface integral to pixels on the IV area. Assuming

that \mathbf{g} is fixed, we obtain the Fredholm integral equation of the first kind

$$f_p(t) = \int d\Omega W_{\mathbf{g}}(t, \theta, \phi) m(\theta, \phi). \quad (4)$$

Discretization of the time $t \rightarrow t_i$ and planetary surface $(\theta, \phi) \rightarrow (\theta_j, \phi_j)$ reduces the equation (4) to the linear inverse problem

$$d_i = \sum_j W_{ij} m_j, \quad (5)$$

or using the vector form, we can express it as

$$\mathbf{d} = W\mathbf{m}, \quad (6)$$

where $d_i = f_p(t_i)$ for $i = 0, 1, \dots, N_i - 1$ and $m_j = m(\theta_j, \phi_j)$ for $j = 0, 1, \dots, N_j - 1$. The explicit expression of the geometric kernel $W_{ij} = W_{\mathbf{g}}(t_i, \theta_j, \phi_j)$ in the spherical coordinate is given in Appendix A.

Because the inverse problem (6) is ill-posed, an additional constraint or regularization is needed to solve the problem. Various types of regularizations have been attempted so far. Kawahara & Fujii (2010) used non-negative regularization, and the requirement of an upper limit of albedo as regularization using the bounded variable least squares solver (Lawson & Hanson 1995). Kawahara & Fujii (2011) used the Tikhonov regularization, which minimizes the cost function

$$\text{minimize } Q = \frac{1}{2} \|\mathbf{d} - W\mathbf{m}\|_2^2 + \frac{\lambda_A}{2} \|\mathbf{m}\|_2^2, \quad (7)$$

where λ_A is the spatial regularization parameter and $\|\cdot\|_2^2$ is the squared L2 norm. To construct the model on the Bayesian framework, Farr et al. (2018) used a Gaussian process to regularize the map while Berdyugina & Kuhn (2019) used an Occamian approach algorithm. Recently, Aizawa et al. (2020) demonstrated that the L1 + total square variation (TSV) provided better results than a simple L2 (Tikhonov) regularization.

The value of \mathbf{d} depends on what features we want to extract from the multi-color light curve. Kawahara & Fujii (2011) used a single-band light curve to retrieve a cloud map of the simulated Earth. They also demonstrated that a rough two-dimensional distribution of the continent or ocean can be retrieved from a color difference between 0.85 micron and 0.45 micron or 0.85 micron and 0.65 micron, owing to the near flatness of the cloud spectrum. Cowan et al. (2009) utilized principle component analysis (PCA) for their longitudinal mapping of EPOXI data. Fan et al. (2019) used the second component of PCA of the multi-color light curve of DSCOVR. Comparing with the ground truth, they found that the resultant map was similar to the global

continent/ocean map of the Earth. However, these two examples required prior knowledge of the surface composition or the ground truth of the geography. The ambiguity in the interpretation of the map is a limitation of the spin-orbit tomography.

2.2. Spectral Unmixing

Spectral unmixing is a procedure that disentangles mixed spectra by finding the endmembers. The mixing model of the spectra of multiple surface compositions is required to unmix the spectra. The simplest model is the linear mixing model, expressed as

$$d(t_i, \tilde{\lambda}_l) = D_{il} = \sum_k A_{ik} X_{kl}, \quad (8)$$

or simply

$$D = AX, \quad (9)$$

where $A_{ik} = a_k(t_i)$ is the contribution of the k -th component at time $t = t_i$ to the intensity of light and $X_{kl} = x_k(\tilde{\lambda}_l)$ for $l = 0, 1, \dots, N_l - 1$ is the reflection spectra of the k -th component at wavelength $\tilde{\lambda}_l$ ¹. We need to solve the matrix factorization of A and X . Generally, the matrix factorization is formulated as the minimization of the cost function, where the cost function can either be the squared Euclidean distance or the Kullback–Leibler distance. In this paper, we use the squared Euclidean distance

$$Q = \frac{1}{2} \|D - AX\|_F^2 + R(A, X) \quad (10)$$

where $\|\cdot\|_F^2$ is the squared Frobenius norm defined by

$$\|Y\|_F^2 \equiv \sum_j \sum_i Y_{ij}^2. \quad (11)$$

and $R(A, X)$ is the regularization term.

2.2.1. Principle Component Analysis

Principle component analysis (PCA) is a traditional technique used to disentangle the spectral components of multi-color light curves as observed in Cowan et al. (2009). It was also used in a global map reconstruction of the Earth by Fan et al. (2019) and Aizawa et al. (2020). PCA can also be formulated as a minimization

¹ We note that the spectral unmixing in remote sensing is often expressed in the form of $D' = X'(A')^T$ instead of equation (9), i.e. “spectral component first”, where $D' = D^T$, $X' = X^T$, $A' = A$. We select the form of equation (9) because of the connectivity between the unmixing and spin-orbit tomography as seen in section 2.3.

of the cost function, from the perspective of optimization,

$$\text{minimize } Q = \frac{1}{2} \|D - AX\|_F^2 \quad (12)$$

$$\text{subject to } A^T A = \text{diag}(\sigma_A) = \Sigma_A, \quad (13)$$

$$X^T X = \text{diag}(\sigma_X) = \Sigma_X, \quad (14)$$

where $\text{diag}(\sigma)$ is a diagonal matrix whose elements are σ_i . The drawback of the PCA as a matrix factorization method is the strong assumption of orthogonality for A and X . However, its orthogonality is useful to visualize the simplex by reducing its dimensionality (Cowan & Strait 2013). In this paper, we denote the orthogonal PCA basis by $U_X = (\Sigma_X^{-1/2} X)^T$, i.e. $U_X^T U_X = I$ (I is an identity matrix). An arbitrary matrix M can be decomposed by row vectors of U_X as

$$M = \sum_k \mathbf{p}_k \mathbf{u}_k^T, \quad (15)$$

where \mathbf{u}_k is the k -th row of U_X . The projection of M on to $\text{PC}k$ is computed by

$$\mathbf{p}_k = M \mathbf{u}_k. \quad (16)$$

2.2.2. Non-negative Matrix Factorization

In the field of remote sensing, a wide variety of spectral unmixing has been studied. Among these techniques, NMF decomposes a single matrix D to two matrices A and X whose elements are non-negative, that is, $D = AX$ (Paatero & Tapper 1994; Lee & Seung 2001). NMF can be defined by the minimization of the cost function. For instance, using the squared Euclidean distance, NMF is formulated as

$$\text{minimize } Q = \frac{1}{2} \|D - AX\|_F^2 + R(A, X) \quad (17)$$

$$\text{subject to } A_{ik} \geq 0, X_{kl} \geq 0. \quad (18)$$

NMF is known to be NP-hard (Vavasis 2009), therefore, the optimization of NMF is difficult to achieve. Nevertheless, various efficient optimization methods have been proposed (Lee & Seung 2001; Cichocki et al. 2009, references therein).

In particular, NMF combined with the simplex volume minimization technique can accurately reproduce the high-resolution spectrum components from remote-sensing satellite data (Craig 1994; Fu et al. 2015; Lin et al. 2015; Fu et al. 2019; Ang & Gillis 2019). The concept of the simplex volume minimization is summarized as follows: If the data are sufficiently spread in the convex hull defined by the endmembers, the data-enclosing simplex whose volume is minimum identifies the true endmembers.

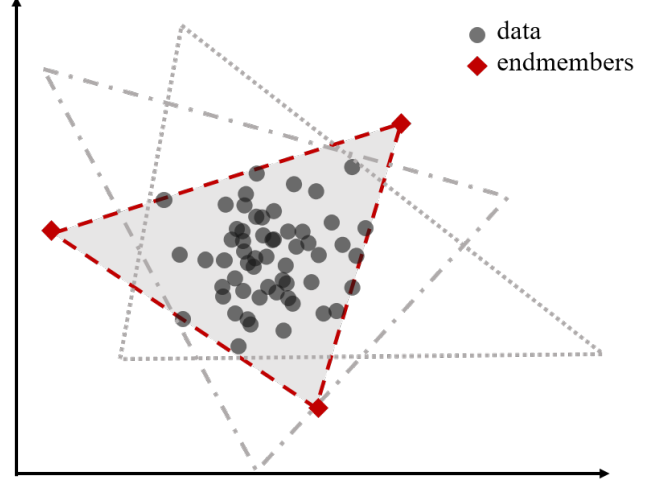


Figure 1. Schematic picture of the simplex volume minimization, which is based on Figure 1 in Lin et al. (2015) (see also Fujii et al. 2017). Black dots represent observed data and three triangles indicate a simplex that encloses all the data points. The dashed triangle is the simplex whose volume is minimum. The endmembers are defined by three vertices of the dashed triangle.

In Figure 1, we plot three simplexes that enclose all the data points. Each simplex provides its vertices as a solution of NMF. The simplex volume minimization chooses the vertices of the volume-minimum simplex (dashed triangle) as the endmembers of NMF. When there is at least one pure pixel of each endmember in the data, the volume-minimum simplex obviously identifies the true endmembers. Even in the case without pure pixels, Lin et al. (2015) showed that the true endmembers could be identified by the volume-minimum simplex under the condition of the pixel purity level that applies uniformly to all the endmembers. In Figure 1, if the data points on the red dashed lines have high purity level, that is, these are on the boundaries of the simplex defined by the true endmembers, the volume-minimum simplex identifies the true endmembers.

As the regularization term for the simplex volume minimization, the Gram determinant of spectral components (VRDet)

$$R(A, X) = \frac{\lambda_X}{2} \det(X X^T) \quad (19)$$

$$= \frac{\lambda_X}{2} \det_{k,k'} \left[\sum_l (X_{kl} X_{k'l}) \right], \quad (20)$$

was used (e.g. Schachtner et al. 2009; Zhou et al. 2011; Xiang et al. 2015; Fu et al. 2019; Ang & Gillis 2019), where λ_X is the spectral regularization parameter. The Gram determinant (19) is a surrogate of the volume of a

convex hull of spectral vectors, $(\mathbf{x}_0, \mathbf{x}_1, \dots, \mathbf{x}_{N_k-1})$, where $\mathbf{x}_k = \{x_k(\tilde{\lambda}_l) \text{ for } l = 0, 1, \dots, N_l - 1\}$; such a convex hull is identifiable for its well-spread data (Lin et al. 2015)². The minimization of the convex hull of spectral vectors can be achieved by minimizing (19).

2.3. Unified Retrieval Method of Mapping and Spectra

Our task is to unify the spectral unmixing (9) and spin-orbit tomography (6). To achieve this, we assume a pixel-wise spectral unmixing

$$m(\theta_j, \phi_j, \tilde{\lambda}_l) = m_{jl} = \sum_k A_{jk} X_{kl}, \quad (21)$$

where X_{kl} is the reflectivity of the k -th component at wavelength $\tilde{\lambda}_l$, and $A_{jk} = a_k(\theta_j, \phi_j)$ is the surface distribution of the k -th surface component at the j -th pixel instead of time in equation (9). Combining equation (21) with the multi-color version of equation (6), we obtain

$$D_{il} = \sum_j W_{ij} m_{jl} = \sum_{jk} W_{ij} A_{jk} X_{kl} \quad (22)$$

or simply,

$$D = WAX. \quad (23)$$

Equation (23) provides the general form of the spin-orbit tomography with spectral unmixing.

The two-dimensional mapping thus far estimated the spectra using PCA or a color difference prior to retrieving the geographic distribution. This “unmixing first” strategy could not feedback information on the fitting accuracy of the geographic retrieval to spectral unmixing. The improvement of Equation (23) over the spin-orbit tomography is that we fit both the spectral components and geography to data in a consistent manner.

Cowan & Strait (2013) solved an equation similar to (23) for A and X using the multi-color light curve provided by the EPOXI satellite as D . They retrieved a longitudinal map of the surface components from the diurnal rotation of the light curve. This procedure is referred to as “rotational unmixing”. They used the Markov chain Monte Carlo method to determine the best parameters of X and D . Their optimization corresponds to the minimization of

$$Q = \frac{1}{2} \|D - \bar{W}AX\|_F^2 \quad (24)$$

$$\text{subject to } 1 \geq \sum_k A_{jk} \geq 0, 1 \geq X_{kl} \geq 0, \quad (25)$$

²

The Gram determinant can be rewritten by the wedge product of the spectral vectors as $\det(XX^T) = \|\mathbf{x}_0 \wedge \mathbf{x}_1 \wedge \dots \wedge \mathbf{x}_{k-1}\|^2$. Therefore, $\det(XX^T)$ can be regarded as the squared volume of the spectral vectors.

where \bar{W} is the latitudinal average of the kernel³. The minimization of equation (24) under the constraint of (25) is formally identical to the weighted NMF (we explain this in §2.4) with no regularization + the upper limits of A and X .

In general, matrix factorization has a degeneracy of solutions. The transformation of $A \leftarrow AG^{-1}$, and $X \leftarrow GX$ for a regular matrix G under the constraint (25) does not change the value of the cost function (24). This means that if we change the spectral basis by a rotation of G , then the inferred map should change too. This degeneracy is known in the field of blind signal separation (e.g. see Chapter 1.3.2 in Cichocki et al. 2009). The non-uniqueness of the blind signal separation might explain the mismatch between the inferred longitudinal map by Cowan & Strait (2013) and the actual geography suggested by Fujii et al. (2017).

The non-uniqueness feature of NMF can be avoided by adding regularization when neglecting unavoidable scaling and permutation ambiguities (Cichocki et al. 2009; Lin et al. 2015). Our task is to find a unique (identifiable) solution to the spectral unmixing and spin-orbit tomography. To achieve this, we consider the cost function with regularization for both X and A . In this paper, we used the squared Euclidean distance as the cost function for equation (23)

$$Q = \frac{1}{2} \|D - WAX\|_F^2 + R(A, X) \quad (26)$$

where $R(A, X)$ is the regularization term. Similar to the rotation unmixing for longitudinal mapping (Cowan & Strait 2013), we call the two-dimensional mapping+unmixing+regularization (26) spin-orbit unmixing in this paper.

2.4. Weighted Nonnegative Matrix Factorization

The non-negative condition of the equation (26) yields an NMF version of the unified retrieval model

$$\text{minimize } Q = \frac{1}{2} \|D - WAX\|_F^2 + R(A, X) \quad (27)$$

$$\text{subject to } A_{jk} \geq 0, X_{kl} \geq 0. \quad (28)$$

As this formulation differs from a standard NMF (17) for a weight W , we require an extension for the optimization of a standard NMF to the weighted NMF.

³ Aside the additional constraints on X and A , the difference between the equation in Cowan & Strait (2013) and equation (23) is the W . As rotational unmixing does the longitudinal mapping according to spin rotation, the geometric kernel should be integrated unto the latitudinal direction, $\bar{W} = \bar{W}(\phi)$. In the frame of the spin-orbit tomography, we need to use a 2-dimensional discretization of a sphere, $W(\theta, \phi)$.

2.4.1. Regularization

The regularization term suppresses the instability of the retrieved map due to overfitting, otherwise known as overtraining in machine learning. A Tikhonov regularization (or a L2 regularization) used in the original spin-orbit tomography (Kawahara & Fujii 2011) can be extended to the regularization term using the Frobenius norm, $R(A, X) \propto \|A\|_F^2$. Hence, a simple extension of the spin-orbit tomography is expressed as

$$R(A, X) = \frac{\lambda_A}{2} \|A\|_F^2 \quad (\text{L2-Unconstrained}). \quad (29)$$

However, in the case of “L2”, we do not have any regularization for X (“L2-Unconstrained”). In spectral unmixing, an assumption made on the convex hull of spectral components can be expressed as a regularization term (a function of X), as explained in Section 2.2.2. We consider a combination of the Tikhonov regularization for mapping, and the Gram determinant-type volume regularization for spectral components, expressed as

$$R(A, X) = \frac{\lambda_A}{2} \|A\|_F^2 + \frac{\lambda_X}{2} \det(XX^T) \quad (\text{L2-VRDet}), \quad (30)$$

where λ_A and λ_X are the regularization parameters for A and X , respectively. We call this model “L2-VRDet”.

2.4.2. Optimization

The minimization of the cost function is performed by a block coordinate descent, which consists of two separate optimizations for A and X (see Kim et al. 2014, as a review paper). These optimizations are solved by minimizing the quadratic forms

$$q_A = \frac{1}{2} \mathbf{a}_k^T \mathcal{W}_A \mathbf{a}_k - \mathbf{b}_A^T \mathbf{a}_k \quad (31)$$

$$q_X = \frac{1}{2} \mathbf{x}_k^T \mathcal{W}_X \mathbf{x}_k - \mathbf{b}_X^T \mathbf{x}_k. \quad (32)$$

of \mathbf{a}_k (the k -th column vector of A) and \mathbf{x}_k (the k -th row vector of X) for $k = 0$ to $N_k - 1$, iteratively (Zhou et al. 2011), where $\mathcal{W}_A, \mathcal{W}_X, \mathbf{b}_A$, and \mathbf{b}_X are placeholders that depend on the cost function.

As the L2 regularization of A , we minimize

$$q_A = \frac{1}{2} \mathbf{a}_k^T (\mathcal{L}_A + \mathcal{T}_A) \mathbf{a}_k - \mathbf{l}_A^T \mathbf{a}_k \quad (\text{L2}) \quad (33)$$

$$\mathcal{L}_A = \mathbf{x}_k^T \mathbf{x}_k W^T W \quad (34)$$

$$\mathbf{l}_A = W^T \Delta \mathbf{x}_k \quad (35)$$

$$\mathcal{T}_A = \lambda_A I_J \quad (36)$$

where $\Delta_{il} = D_{il} - \sum_{s \neq k} \sum_j W_{ij} A_{js} X_{sl}$, $I_J \in \mathbb{R}^{N_j \times N_j}$ is an identity matrix. The X component of the quadratic

problem for the VRDet model is calculated by

$$q_X = \frac{1}{2} \mathbf{x}_k^T (\mathcal{L}_X + \mathcal{D}_X) \mathbf{x}_k - \mathbf{l}_X^T \mathbf{x}_k \quad (\text{VRDet}), \quad (37)$$

$$\mathcal{L}_X = \|W \mathbf{a}_k\|_2^2 I_L \quad (38)$$

$$\mathbf{l}_X = \Delta^T W \mathbf{a}_k \quad (39)$$

$$\mathcal{D}_X = \lambda_X \det(\check{X}_k \check{X}_k^T) [I_L - \check{X}_k^T (\check{X}_k \check{X}_k^T)^{-1} \check{X}_k], \quad (40)$$

where \check{X}_k is a submatrix of X when the k -th row of X is removed and $I_L \in \mathbb{R}^{N_l \times N_l}$ is the identity matrix. The derivations of these terms are given in Appendix B.1.

Following Ang & Gillis (2019), we use the accelerated projected gradient descent + restart (APG+restart) to optimize the quadratic problems with non-negative conditions. The APG+restart is based on a projected gradient descent onto a positive orthant with Nesterov’s acceleration and the restarting method. The algorithm is summarized as follows.

Algorithm: NMF/Block Coordinate Descent for Spin-Orbit Unmixing

```

Minimize  $\frac{1}{2} \|D - WAX\|_F^2 + R(A, X)$  s.t.  $A, X \geq 0$ 
Initialize  $A^{(0)}, X^{(0)}$  by random nonnegative values
while Condition do
  for  $k$  in  $(0, N_k - 1)$  do
    Update  $\mathbf{x}_k$  using APG+restart
    Update  $\mathbf{a}_k$  using APG+restart
  end for
end while

```

A more detailed description of the APG+restart algorithm is given in Appendix B.2. Additionally, we show that the traditional multiplicative update algorithm is extended for the weighted NMF in Appendix C. The code for optimization is publicly available⁴.

3. TESTING THE SPIN-ORBIT UNMIXING USING A CLOUDLESS TOY MODEL

We test the spin-orbit unmixing by using the volume-regularized NMF and applying it to a toy model. The toy model assumes three surface types on a planet, including ocean, land, and vegetation. The reflection spectra for land and vegetation were taken from the ASTER spectral library (Baldridge et al. 2009), and the ocean albedo is from McLinden et al. (1997), as indicated by gray lines in Figure 2. The input classification of the map is based on the moderate resolution imaging spectroradiometer classification map in 2008, as shown in

⁴ <https://github.com/HajimeKawahara/sot>

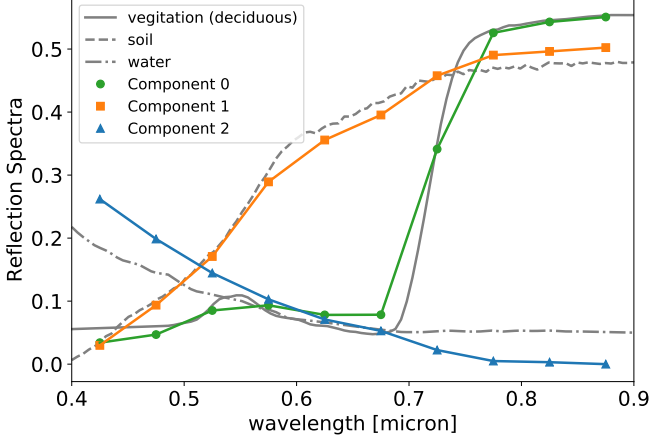


Figure 2. Input (gray) and unmixed spectral components (color with markers) for the L2-VRDet model with $\lambda_A = 10^{-1}$ and $\lambda_X = 10^2$.

the left panel in figure 3. We use the geometric settings of Fujii & Kawahara (2012), an orbital inclination of 45° , obliquity of 23.4° , and $\Theta_{\text{eq}} = 90^\circ$. We assume the spin rotation period is a sidereal day of Earth, $23.9344699/24.0$ d and an orbital revolution period P_{orb} of 365 d. We took $N_i = 512$ homogeneous samples over a year and injected a 1 % Gaussian noise into the light curve.

For the retrieval, we use a HEALPix map (Górski et al. 2005) as A_{jk} with $j = 1, 2, \dots, N_{\text{pix}} = 3072$ pixels. In this test, we assume that we know the number of spectral components, $N_k = 3$. Furthermore, we assume that we know the axial tilt parameters \mathbf{g} and set 10^5 as the number of iterations for the optimization.

Figures 2 and 4 are examples of unmixed spectra and retrieved maps for the L2-VRDet model ($\lambda_A = 10^{-1}$ and $\lambda_X = 10^2$). Because the normalization of each component is arbitrary, we adjust the normalization of each component to the input spectra. In this case, the input spectra and geography are accurately reproduced by the unmixed spectra and their retrieved distributions of components 0, 1, and 2, which corresponds to vegetation, land, and water, respectively. These results indicate that the spin-orbit unmixing using the volume-regularized NMF can infer the spectral components and their geography simultaneously.

The sparsity of the retrieved maps is a notable feature of the spin-orbit unmixing that utilizes NMF. Because of the non-negative constraint, large parts of the maps remain zero. This feature was observed in the spin-orbit tomography using BVLS in Kawahara & Fujii (2010). In contrast, the spin-orbit tomography that uses the Tikhonov regularization does not exhibit such sparsity (Kawahara & Fujii 2011).

We made a color composite map from the three maps in Figure 4, as shown in the right panel of Figure 3. These results show that the L2-VRDet model with an appropriate regularization can infer a global composition map for the toy model.

We remind the reader that the spectra are well mixed even for the cloudless toy model. To illustrate how the spectra are unmixed, we project the input light curves and unmixed spectra as end members onto the PC1 – PC2 plane in Figure 5. The PCA is computed using the input light curve. To draw this plot, we first compute the normalized light curve via the mixing matrix $\tilde{A} \equiv WA$, that is

$$D = \tilde{A}X. \quad (41)$$

The light curve is normalized as $\tilde{D}_{il} = D_{il} / \sum_k \tilde{A}_{ik}$. We then derive PC1 and PC2 using \tilde{D}_{il} . The projection of \tilde{D}_{il} and X onto the PC1–PC2 plane, indicated by the orange crosses and red points, was computed using equation (16). The light curve does not touch the boundary of the triangle, which is defined by end members, that is, the triangle is not a convex hull of the light curve. This is because the spectra of the light curve are well mixed and the purity is low. In this case, the geometric disentanglement is essential for the spectra unmixing because the endmembers are far from the trajectory of the light curves. The “disentangled spectra” of the light curve are defined by $\tilde{X} \equiv AX$, that is

$$D = W\tilde{X}. \quad (42)$$

The blue dots are the projection of the disentangled spectra normalized by $\sum_k A_{jk}$ onto the PC1–PC2 plane. The disentangled spectra are well spread in the triangle, and therefore, the triangle defines a convex hull of the disentangled spectra. The effect of the geometric disentanglement of the spectral unmixing is visualized as the expansion from orange crosses to blue dots in Figure 5.

3.1. Dependence on Regularization Parameters

The over-regularization of the simplex volume (i.e. large λ_X) induces a worse fit of the data. This is confirmed by the mean residual of fitting the model to the data.

$$\text{mean residual} \equiv \frac{1}{\bar{D}} \sqrt{\frac{\|D - WAX\|_F^2}{N_l N_i}}, \quad (43)$$

where \bar{D} is the mean value of the data. The top panel of Figure 6 presents the mean residual as a function of λ_X . The mean residual gradually increases as the spectral regularization parameter increases. $\lambda_X = 10^{-2}$ and 10^{-1} have similar mean residuals, which indicates

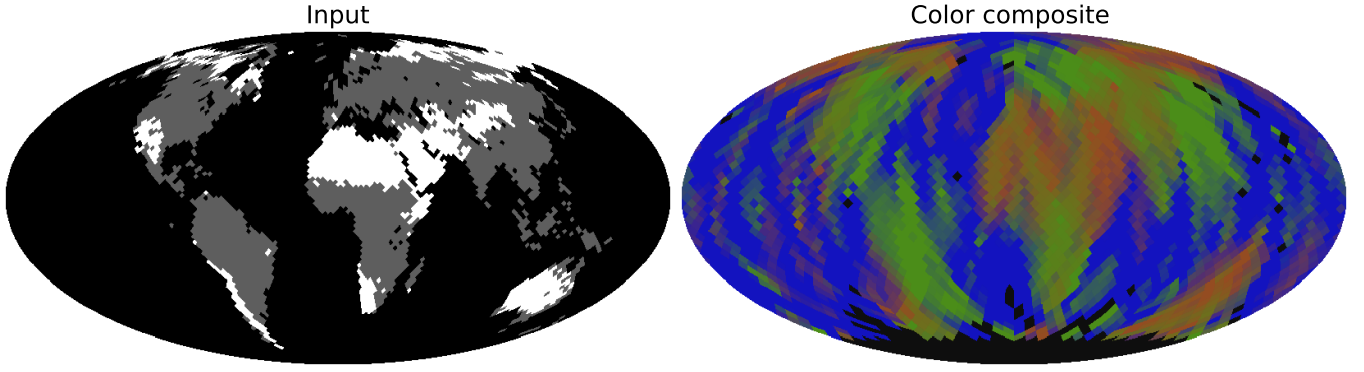


Figure 3. Left: Input map of a toy model. Three colors indicate different surface types, land, vegetation, and ocean corresponding to white, gray, and black. Right: Color composite map for the same model. The color composite is based on the retrieved components in Figure 2; the component 0, 1, and 2 correspond to green, orange, and blue, respectively.

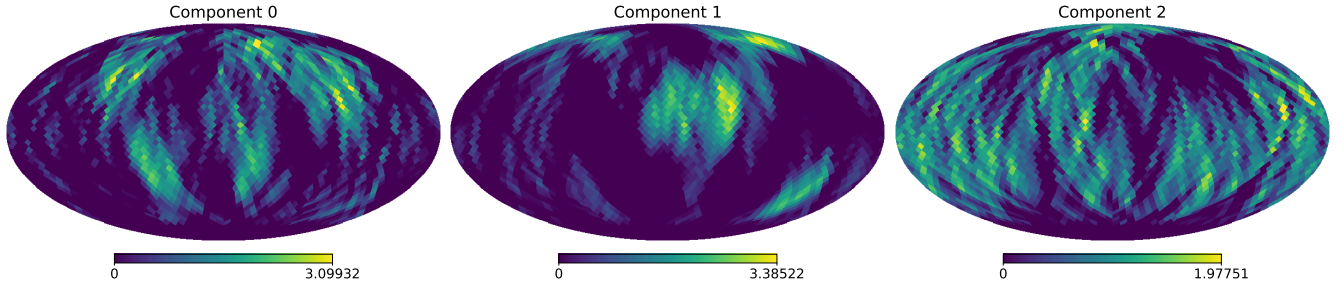


Figure 4. Retrieved maps for different unmixed components 0, 1, and 2 from left to right. We adopt L2-VRDet model with $\lambda_A = 10^{-1}$ and $\lambda_X = 10^2$.

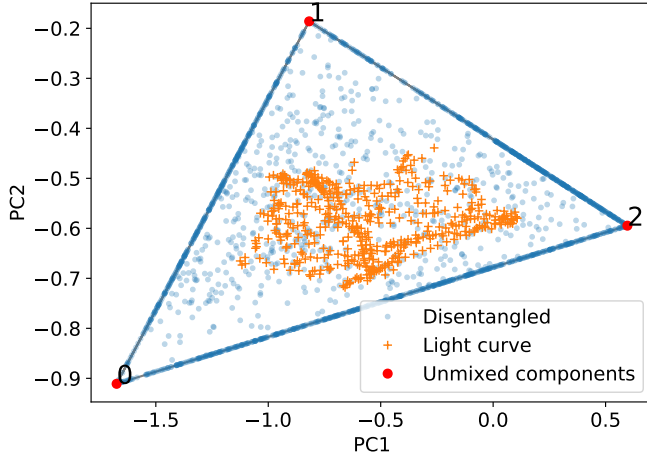


Figure 5. Input light curve (orange cross), unmixed spectral components (red points), disentangled spectra (blue dots) on the PC1 – PC2 plane. A simplex defined by the components 0, 1, and 2 are shown by the gray triangle.

that the model fits the data well for small regularization parameters. A smaller spectral regularization provides fewer constraints on the simplex volume minimization. Hence, there is a trade-off relation between the models goodness of fit and volume minimization.

The panel below the top one illustrates a surrogate of the spectral of volume of normalized spectral components $\det(\hat{X}\hat{X}^T)$, where $\hat{X}_{kl} = X_{kl}/\sum_l X_{kl}$. This quantity decreases as the spectral regularization parameter increases, which indicates that the spectral volume is minimized more as λ_X increases. The surrogate of the normalized spectral volume roughly converges at $\lambda_X = 10^1$.

The direct comparison with the ground truth is useful to see how λ_X affects the estimate of the spectral components and geography. To quantify the difference between the unmixed spectra and ground truth, we define the mean removed spectral angle (MRSA) between the two vectors \mathbf{x} and \mathbf{y} as

$$\text{MRSA}(\mathbf{x}, \mathbf{y}) = \frac{1}{\pi} \cos^{-1} \left(\frac{(\mathbf{x} - \bar{\mathbf{x}})^T (\mathbf{y} - \bar{\mathbf{y}})}{\|\mathbf{x} - \bar{\mathbf{x}}\|_2 \|\mathbf{y} - \bar{\mathbf{y}}\|_2} \right), \quad (44)$$

where $\bar{\mathbf{x}}$ and $\bar{\mathbf{y}}$ are the mean of \mathbf{x} and \mathbf{y} respectively, and $\text{MRSA}(\mathbf{x}, \mathbf{y}) \in [0, 1]$. The two vectors perfectly match when the $\text{MRSA}(\mathbf{x}, \mathbf{y}) = 0$. The third panel shows the mean of MRSA over the components

$$\overline{\text{MRSA}} = \sum_k \text{MRSA}(\mathbf{x}_k, \mathbf{x}_k^G) / N_k, \quad (45)$$

where $\mathbf{x}_k^{\mathcal{G}}$ is the ground truth (input spectrum). Moreover, figure 7 shows the actual shapes of the unmixed spectra for different λ_X . The difference is observed for Component 2 (orange, land). The unmixed spectra when $\lambda_X \leq 10^0$ resulted in a worse fit to the ground truth. Interestingly, when $\lambda_X \geq 10^3$, the fit of the unmixed spectra to the ground truth also worsened. This is possibly due to the over-constraint on the spectral model which in turn restricts its ability to explain the data accurately (large residuals); this results in an incomplete estimate of the spectral components.

The comparison between the retrieved map and ground truth is quantified by the Correct Pixel Rate (CPR), which is defined by the correct answer rate of the classification map. The bottom panel of figure 6 shows its dependence on λ_X . Insufficient spectral regularization resulted in not only a worse mean MRSA, but also a worse estimate of the geography. In regards to both the mean MRSA and CPR, an optimal range of λ_X is 10^1 – 10^3 was observed.

Although we cannot compute the MRSA and CPR for unknown geographies and surface spectra, these results suggest that a curve of a surrogate of normalized spectral volume, as a function of λ_X , can be used to determine the optimal value of λ_X . We suggest the following procedure: 1) Plot the mean residual and $\det(\hat{X}\hat{X}^T)$ as a function of λ_X . 2) Observe the change of the spectral shape as a function of λ_X . 3) Use λ_X at a turning point of the spectral shape and $\det(\hat{X}\hat{X}^T)$ and avoid a large value for the mean residual.

Figure 8 shows a similar plot to Figure 6, but for the spatial regularization λ_A . The over-constraint on A (i.e. large λ_A) contributes to a bad fit of data and a smaller volume of spectral components. Smaller spatial regularization parameters resulted in a bad estimate of the geography, as indicated by the CPR. This is because insufficient spatial regularization creates a noisy map due to the instability of the mapping (see Figure 9 as an example). Contrastingly, a large λ_A will slightly decreases the CPR because it will imply that the inferred spectra are getting worse and the spatial resolution of the map is decreasing in quality. This poor resolution will result in a large mean residual. Therefore, one should check both the residual and the surrogate of normalized spectral volume as a function of λ_A because these quantities have a trade-off relation. We suggest choosing the optimal λ_A as the smallest value that 1) keeps the noise in the inferred map non-significant and 2) avoids a large mean residual.

We have described how spatial and spectral regularization parameters affect the results; we have also discussed a guideline to follow when choosing the optimal

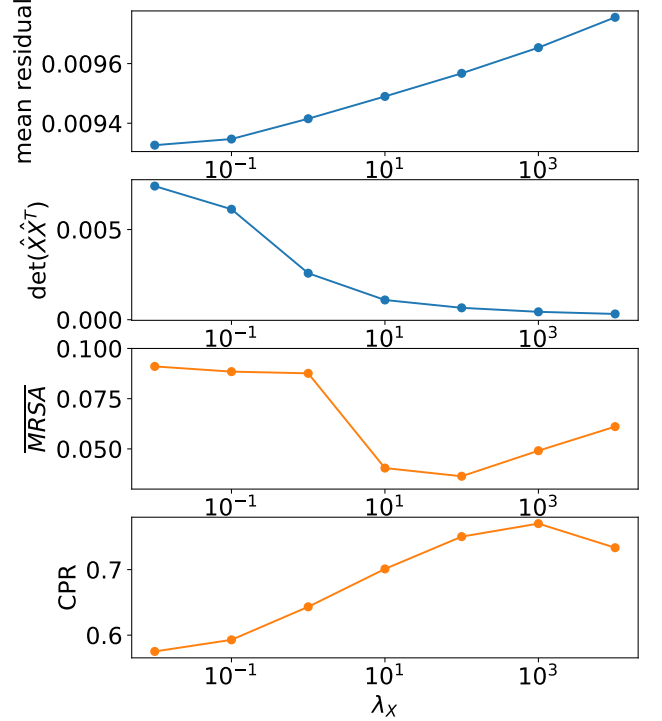


Figure 6. The residuals, the surrogate of the normalized spectral volume, mean MRSA, and CPR as a function of λ_X from top to bottom. We fix $\lambda_A = 10^{-1}$ in these panels.

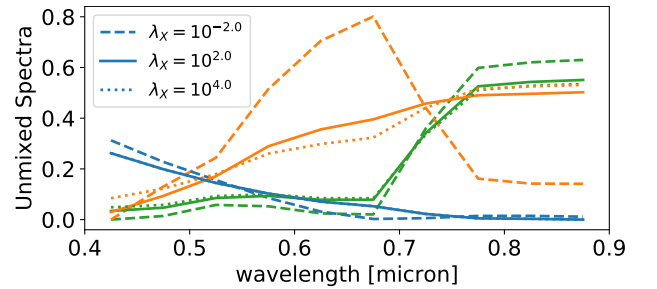


Figure 7. Unmixed spectra for $\lambda_X = 10^{-2}, 10^2$, and 10^4 . The color is the same as Figure 2. We fix $\lambda_A = 10^{-1}$ in these panels.

spatial and spectral parameters. To find the optimal λ_X (or λ_A), we fixed λ_A (or λ_X) in Figure 6 (or Figure 8). In practice, this procedure should be iterative so that we can find the optimal set of λ_A and λ_X . We recognize that our current guideline for choosing the optimal parameters is not quantitative. Ideally, the performance of the prediction can be used to choose the optimal parameters, such as cross-validation. However, the large computational time of the optimization method is too long to do a cross-validation. Therefore, we postpone

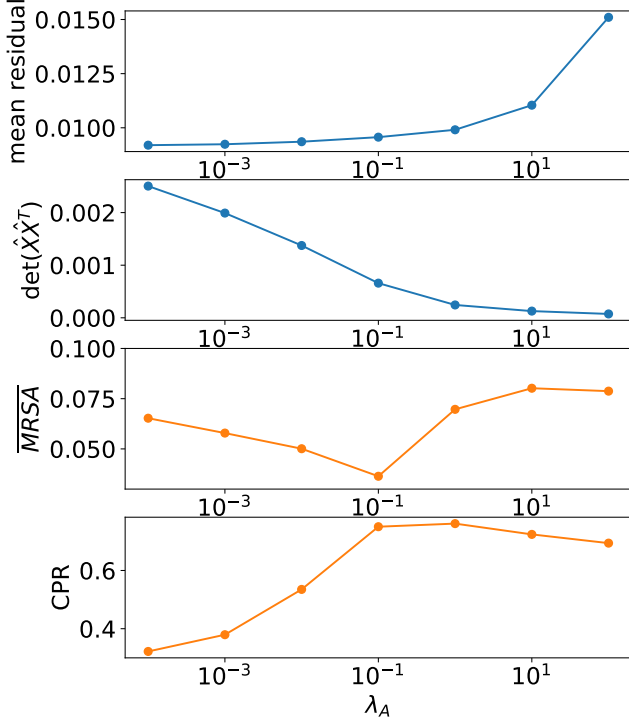


Figure 8. Mean residual, a surrogate of the normalized spectral volume, mean MSRA and CPR as a function of λ_A from top to bottom. We fix $\lambda_X = 10^2$ in these panels.

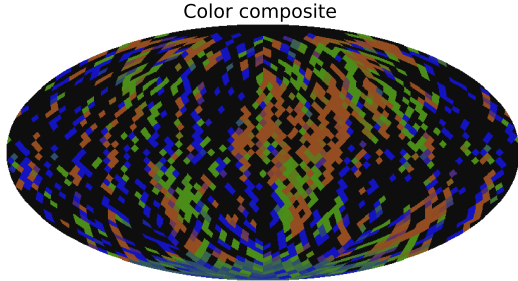


Figure 9. Example of the color composite map for insufficient spatial regularization ($\lambda_A = 10^{-3}$). We adopt $\lambda_X = 10^2$ to make this figure.

the quantitative criterion needed to choose the parameters for further study.

3.2. Choice of the Number of Spectral Components

So far, we have assumed the number of spectral components $N_k = 3$. Generally, N_k should be one of the free parameters. Here, we consider the cases for when $N_k = 2$ (over-constrained) and $N_k = 4$ (under-constrained). The cost function for $N_k = 2$ ($Q = 6 \times 10^4$) is much larger than that of $N_k = 3$ ($Q = 2355$) and 4 ($Q = 2565$). This indicates that $N_k = 2$ is insufficient to

explain the data. For $N_k = 4$, we could not reach the convergence of the cost function (26) with the regularization term (30) even though the number of iterations reached 10^6 which was where we stopped.

Although information criterion such as Akaike Information Criterion (AIC) is used as the model selection for a different number of free parameters, the degree of freedom is not clear for the inverse problem. Ignoring this fact, if we evaluate AIC by $-2\log(\text{Likelihood}) + 2(\text{degree of freedom}) = \|D - WAX\|_F^2/\sigma^2 + 2N_k N_j$, where σ is the standard deviation of the input noise, we obtain AIC = 135158.8, 23141.4, and 28889.3 for $N_k = 2, 3$, and 4, respectively. These results might indicate that $N_k = 3$ is the optimal number for the components.

Another problem in real data is that it is often difficult to estimate the likelihood because we do not understand the statistical nature of the noise. In this case, the cross validation is often used as the model selection. However, the cross validation is unrealistic because of the high computational cost of the current scheme. We postpone the criterion, which will allow us to choose the optimal number of surface components for further study. Hence, in this paper, we require the number of surface components as prior knowledge for mapping.

3.3. Comparison with Spectral Unmixing on Light Curves

So far, we have explained how geography is disentangled from spectra in spin-orbit unmixing. Here, we consider spectral unmixing on the light curve with no disentanglement of geometry and compare it with the unified model. By minimizing the cost function,

$$Q = \frac{1}{2} \|D - \tilde{A}X\|_F^2 + \frac{\lambda_X}{2} \det(XX^T) \quad (46)$$

$$\text{subject to } \tilde{A}_{ik} \geq 0, X_{kl} \geq 0, \quad (47)$$

we obtain the unmixed spectral components for different spectral regularization as shown in Figure 10. We find that both components 0 and 1, which can be interpreted as surface components on continents, are sensitive to the volume regularization. These results show that the NMF with simplex volume minimization works even without geometric disentanglement.

Compared with the spin-orbit unmixing, the spectrum of soil (gray dashed) is less reproduced by the component 1 (orange) even for the best case, $\lambda_X = 10^0$ and the results are more sensitive to the choice of λ_X (see Figure 7 for comparison). This is likely because the geometric disentanglement is essential to sufficiently separate the spectrum of soil from that of vegetation.

4. APPLICATION TO DSCOVER DATA

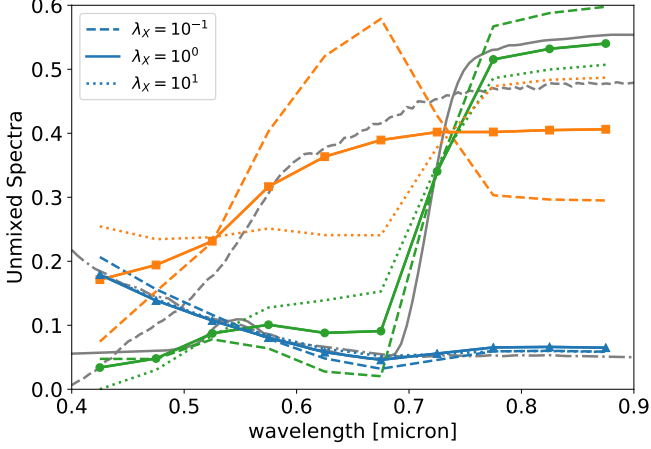


Figure 10. Unmixed spectral components (color with markers) for the direct spectral unmixing of the light curve with $\lambda_X = 10^{-1}, 10^0$, and 10^1 . Green (circle), orange (square), and blue (triangle) correspond to component 0, 1, and 2. The gray lines are input spectra same as Figure 2.

In this section, we demonstrate our method using real multiband light curves of the Earth as observed by DSCOVR (Jiang et al. 2018). DSCOVR has been continuously monitoring our Earth from the L1 point since 2015. The geometry provided by DSCOVR is not the same as the geometry provided by direct imaging because DSCOVR continuously looks almost the dayside of Earth. However, the geometric kernel contains latitudinal information because of the axial tilt of the Earth. This enables us to do a two-dimensional mapping (Fan et al. 2019). We use seven optical bands (0.388, 0.443, 0.552, 0.680, 0.688, 0.764, and 0.779 μm) in DSCOVR filters ($N_l = 7$). The band widths are very narrow (0.8 – 3.9 nm) and there are strong oxygen B and A absorption in 0.688, 0.764 μm . Owing to computational efficiency, we use 1/4 of the two-year data (i.e. one in each four bins) used in Fan et al. (2019), resulting in a number of $N_i = 2435$ time bins.

Figure 12 shows the unmixed spectra and color composite map when we assume that $N_k = 4$. For regularization parameters, we followed the procedure described in the previous section. Figure 11 shows the mean MRSA and surrogate of the normalized spectral volume. It was observed that $\lambda_X = 10^{-2}$ and $\lambda_A = 10^{-4.5}$ are the optimal values because a significant increase of the mean residual is observed at the range larger than these values. Component 1 accurately reproduced the actual geography and blue spectrum of the ocean; components 2 and 3 reproduced the continent distribution of Earth. Component 1 is less sensitive to the choice of λ_X compared with components 2 and 3, therefore, component 1 is a relatively robust estimate of a surface component. From

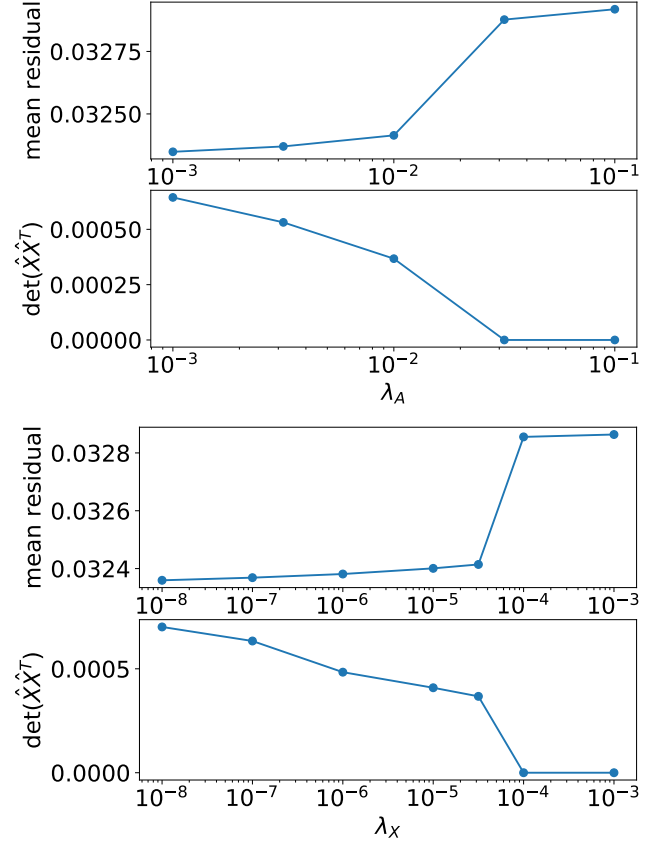


Figure 11. Mean residual and the surrogate of the normalized spectral volume as functions of λ_A (top; $\lambda_X = 10^{-4.5}$) and λ_X (bottom; $\lambda_A = 10^{-2}$). We take 10^{-2} as the optimal value of λ_A because of a significant increase at $\lambda_A = 10^{-1.5}$. Also, we take $10^{-4.5}$ as the optimal value of λ_X because of a significant increase in the mean residual at $\lambda_X = 10^{-4}$.

the unmixed spectrum, component 2 resembled the spectrum of vegetation because of the increase larger than 0.688 micron although the strong oxygen absorption at 0.688 and 0.764 microns suppressed this increase to some extent. Component 3 corresponds to the spectrum of soil or sands. In fact, the continent of Australia (less vegetation) was painted by component 3. The southern part of Africa and the Amazon (large forest areas) are roughly painted by component 2. We do not have enough spatial resolution around North Africa, Eurasia, and Europe. Although we did not consider our scheme being able to clearly distinguish between soil and vegetation, we believe that the differences between components 2 and 3 reflect the variety of spectra of land continents on planet Earth.

Component 0 exhibited a flat spectrum except for strong oxygen absorption bands (0.688, 0.764 μm) reproducing the cloud or ice spectrum. Component 0 as well as component 1 is less sensitive to the choice of

λ_X compared with components 2 and 3. However, the distribution of component 0 is patchy, except for the localization at the North Pole. The patchy distribution probably reflects a temporal cloud distribution because real clouds do not have static distribution, some of which might be from the ice near the pole.

These patchy pixels have values that are roughly $\alpha = 5$ times larger compared to those of other components. Also, the unmixed spectrum of component 0 is $\beta = 50$ times higher on wavelength average than the total value of those of other components. The fraction of the patchy pixels is about $\gamma \sim 1/100$. Multiplying α , β , and γ , we find that the power of component 0 in the patchy pixels is roughly several times higher than the total power of other components. This value is consistent with the contribution of clouds on reflected light on Earth. The fact that the cloud component is localized in these patchy pixels represents a limitation of the current method, which assumes that all the components have a static distribution over the observation period. Further improvement is needed so that non-static components can be included to the model.

5. SUMMARY AND DISCUSSION

In this paper, we constructed a unified retrieval model for spectral unmixing and spin-orbit tomography (spin-orbit unmixing) using the non-negative matrix factorization and L2 and volume regularization. The spin-orbit unmixing works on the cloudless toy model and real multi-color light curves by DSCOVER. Here, we raise several remaining issues that we did not consider in this study as follows.

The simultaneous estimate of the axial tilt parameters \mathbf{g} is first. For simple two-dimensional mapping, Schwartz et al. (2016) analyzed how the axial tilt parameters are inferred from amplitude modulation, and Farr et al. (2018) constructed a Bayesian framework to estimate the parameters. Similar works should also be done in the spin-orbit unmixing. However, the computational cost will be an issue that would need to be addressed as the optimization of NMF needs a high numerical cost.

Moreover, the clock setting problem still remains. Thus far, all the works done on two-dimensional mapping assumes that we know the exact phase of the geometric kernel. The spin rotation period, derived by the auto-correlation function, was assumed to be used (Fujii & Kawahara 2012). However, as Kawahara (2016) pointed out, the apparent periodicity of the photometric variability is not identical to the spin rotation period. The frequency modulation analysis provides the spin rotation period. For instance, we need to check if the spin-orbit unmixing works well when we use an inferred spin

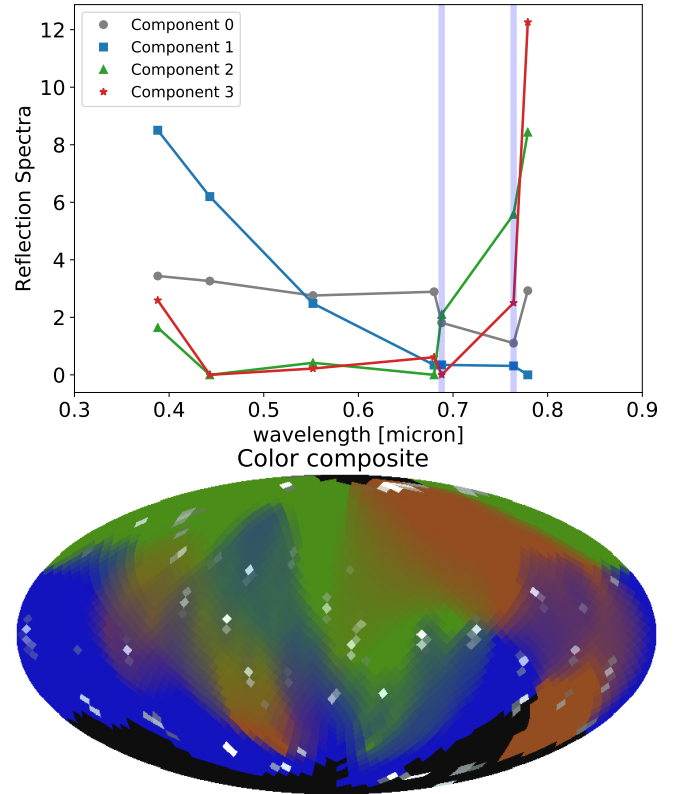


Figure 12. Normalized unmixed spectra (top) and color composite map (bottom) for the DSCOVER data. In the top panel, both 0.688 and 0.764 μm bands are strongly affected by oxygen absorption (shaded by blue vertical lines). The bottom panel shows a color composite map. We use white, blue, green, and brown for components 0, 1, 2, and 3, respectively.

rotation period from the frequency modulation. Otherwise, a technique with a simultaneous estimate of the spin might be required.

The next challenge is how non-static compositions such as clouds can be included in the model (see Luger et al. 2019, as an attempt of the time-dependent mapping.). This will become vitally important when we apply this technique to gaseous planets.

Another challenge is the dependency on results of various types of regularization. For instance, Aizawa et al. (2020) reported that the L1+TSV regularization provided better results than the Tikhonov regularization. Furthermore, several other types of volume regularization have been proposed in the field of remote sensing (e.g. Ang & Gillis 2019); therefore, a comparative study of regularization is required.

Additionally, a more quantitative criterion is needed to select the optimal number of surface components and the regularization parameters. Because of the high computational cost, the cross-validation is unrealistic for the

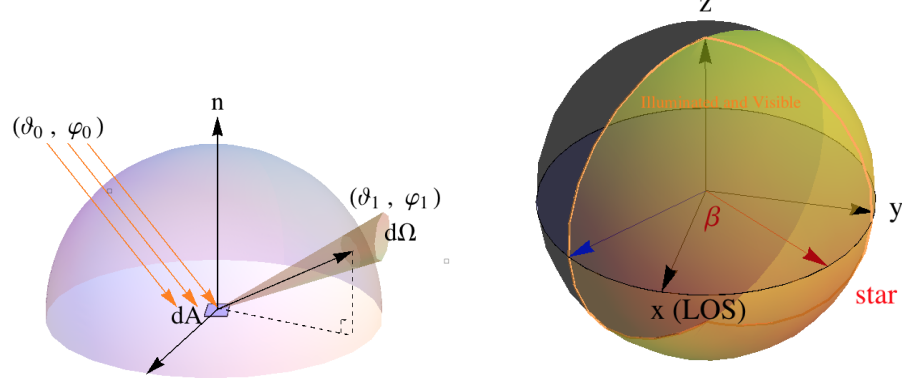


Figure 13. Left: Incoming light and outgoing light of a small facet dA on the surface of a planet. Right: The visible and illuminated (IV) region of a planet surrounded by the orange curve.

current scheme. An objective criterion to select these parameters will help us to apply the technique to unknown exoplanets where the ground truth is not known.

The author is grateful to the DSCOVER team for making the data publicly available. We deeply appreciate Siteng Fan and Yuk L. Yung for providing the processed light curves and their geometric kernel from the DSCOVER dataset. We also thank Masa-

taka Aizawa, Kento Masuda, Nick Cowan for their insightful discussion. We also thank an anonymous reviewer for careful reading and constructive suggestions. This work is supported by JSPS KAKENHI Grant Numbers JP17K14246, JP18H04577, JP18H01247, and JP20H00170. This work was also supported by the JSPS Core-to-Core Program Planet2 and SATELLITE Research from Astrobiology center (AB022006).

APPENDIX

A. GEOMETRIC KERNEL OF THE SPIN-ORBIT TOMOGRAPHY

A.1. Disk-Integrated Scattered Light

Here, we summarize the computation of the reflection light from a planet to an observer. The outward energy from a facet dA to a direction with a solid angle $d\Omega$ (the left panel in Figure 13) is expressed as

$$dE = L_{\uparrow} \cos \vartheta_1 dA d\Omega d\lambda, \quad (\text{A1})$$

where L_{\uparrow} is the upward radiance and ϑ_1 is a zenith angle between a direction and a normal vector. Let us assume that we observe flux from a planet at a distance of d using a telescope with an effective area A_{tel} , then light in a cone with a solid angle $d\Omega = dA_{\text{tel}}/d^2$ contributes to the flux. Therefore, the flux from a facet dA on a plane to the telescope area dA_{tel} is written as

$$\Delta E dA_{\text{tel}} = L_{\uparrow} \cos \vartheta_1 d\Omega dA = \frac{L_{\uparrow}}{d^2} \cos \vartheta_1 dA dA_{\text{tel}}. \quad (\text{A2})$$

Thus, we obtain the total flux from a planet as

$$f_p = \int_{\text{planet}} \Delta E = \int_{\text{planet}} dA \frac{L_{\uparrow}}{d^2} \cos \vartheta_1. \quad (\text{A3})$$

Bidirectional reflectance distribution function (BRDF) of the surface element s is defined by the ratio of the outward radiance to the inward irradiance,

$$R^s(\vartheta_0, \varphi_0, \vartheta_1, \varphi_1) \equiv \pi \frac{L_{\uparrow}(\vartheta_1, \varphi_1)}{E_{\downarrow}(\vartheta_0, \varphi_0)}. \quad (\text{A4})$$

where ϑ_0 and φ_0 are the solar zenith angle and azimuth angle, respectively, and φ_1 is the azimuth angle to an observer (see Figure 13)⁵. For most surface types, the BRDF almost solely depends on a relative azimuth angle $\varphi = \varphi_1 - \varphi_0$ instead of each azimuth angle as

$$R^s(\vartheta_0, \varphi_0, \vartheta_1, \varphi_1) = R^s(\vartheta_0, \vartheta_1, \varphi). \quad (\text{A5})$$

The stellar irradiance is expressed as

$$E_{\downarrow}(\vartheta_0) = \frac{L_{\star}}{4\pi a^2} \cos \vartheta_0 = \frac{f_{\star} d^2}{a^2} \cos \vartheta_0, \quad (\text{A6})$$

where a is the star-planet distance, and L_{\star} and f_{\star} are the stellar luminosity and flux, respectively. The flux from a planet is expressed as

$$\begin{aligned} f_p &= \int_{\text{IV}} dA \frac{E_{\downarrow}(\vartheta_0)}{\pi d^2} R^s(\vartheta_0, \vartheta_1, \varphi) \cos \vartheta_1 \\ &= \frac{f_{\star} R_p^2}{\pi a^2} \int_{\text{IV}} d\Omega_1 R^s(\vartheta_0, \vartheta_1, \varphi) \cos \vartheta_0 \cos \vartheta_1, \end{aligned} \quad (\text{A7})$$

where IV is the illuminated and visible region as shown in the right panel of figure 13.

Assuming an isotropic reflection $R^s(\vartheta_0, \vartheta_1, \varphi) = m(\theta, \phi)$, we obtain,

$$f_p = \int d\Omega_1 W_{\mathbf{g}}(t, \theta, \phi) m(\theta, \phi) \quad (\text{A8})$$

where $W_{\mathbf{g}}(t, \theta, \phi)$ is the geometric kernel for the Lambert approximation.

$$W_{\mathbf{g}}(t, \theta, \phi) = \begin{cases} \frac{f_{\star} R_p^2}{\pi a^2} \cos \vartheta_0 \cos \vartheta_1 & \text{for } \cos \vartheta_0, \cos \vartheta_1 > 0 \\ 0 & \text{otherwise,} \end{cases} \quad (\text{A9})$$

Here, we define the three fundamental vectors, \mathbf{e}_S , \mathbf{e}_O , and \mathbf{e}_R which are the unit vector from the planet center to the stellar center, from the planet center to the observer, and the normal unit vector at the planet surface, respectively. Using them, we can rewrite $\cos \vartheta_0 = \mathbf{e}_S \cdot \mathbf{e}_R$ and $\cos \vartheta_1 = \mathbf{e}_O \cdot \mathbf{e}_R$. Using the orbital phase Θ and an orbital inclination i , we obtain

$$\mathbf{e}_S = (\cos(\Theta - \Theta_{\text{eq}}), \sin(\Theta - \Theta_{\text{eq}}), 0)^T, \quad (\text{A10})$$

$$\mathbf{e}_O = (\sin i \cos \Theta_{\text{eq}}, -\sin i \sin \Theta_{\text{eq}}, \cos i)^T, \quad (\text{A11})$$

where Θ_{eq} is the orbital phase at equinox.

We also define the spherical coordinate fixed on the planet surface,

$$\mathbf{e}'_R(\phi, \theta) = (\cos \phi \sin \theta, \sin \phi \sin \theta, \cos \theta)^T. \quad (\text{A12})$$

Applying a spin rotation along Φ and a rotation matrix $\mathcal{R}(\zeta)$ as a function of a planets obliquity ζ , we get,

$$\begin{aligned} \mathbf{e}_R &= \mathcal{R}(\zeta) \mathbf{e}'_R(\phi + \Phi, \theta) \\ &= \begin{pmatrix} \cos(\phi + \Phi) \sin \theta \\ \cos \zeta \sin(\phi + \Phi) \sin \theta + \sin \zeta \cos \theta \\ -\sin \zeta \sin(\phi + \Phi) \sin \theta + \cos \zeta \cos \theta \end{pmatrix}. \end{aligned} \quad (\text{A13})$$

The geometric weight is given by

$$W_{\mathbf{g}}(t, \theta, \phi) = \begin{cases} \frac{f_{\star} R_p^2}{\pi a^2} (\mathbf{e}_S \cdot \mathbf{e}_R)(\mathbf{e}_R \cdot \mathbf{e}_O) & \text{for } \mathbf{e}_S \cdot \mathbf{e}_R > 0, \mathbf{e}_R \cdot \mathbf{e}_O > 0 \\ 0 & \text{otherwise.} \end{cases} \quad (\text{A14})$$

⁵ We inserted a factor of π so that the BRDF becomes identical to the reflectivity when the scattering is isotropic.

In addition, we consider the case where the reflectivity is constant and isotropic over the surface, $R^s(\vartheta_0, \vartheta_1, \varphi) = R$, (the Lambert approximation). We take $\mathbf{e}_O = (1, 0, 0)^T$ and define the phase angle $\beta = \mathbf{e}_S \cdot \mathbf{e}_O$, i.e. $\mathbf{e}_S = (\cos \beta, \sin \beta, 0)^T$. These definitions yield equation (A7)

$$f_p = \frac{f_\star R_p^2 R}{\pi a^2} \int_{-\pi/2+\beta}^{\pi/2} d\phi \int_0^\pi d\theta \sin^2 \theta \cos \phi (\cos \beta \cos \phi \sin \theta + \sin \beta \sin \phi \sin \theta) \quad (\text{A15})$$

$$= \frac{2R}{3} \phi_p(\beta) \left(\frac{R_p}{a} \right)^2 f_\star, \quad (\text{A16})$$

where

$$\phi_p(\beta) \equiv \frac{1}{\pi} [\sin \beta + (\pi - \beta) \cos \beta], \quad (\text{A17})$$

is the Lambert phase function.

B. OPTIMIZATION OF THE WEIGHTED NMF BY A BLOCK COORDINATE DESCENT

The block coordinate descent (e.g. Kim et al. 2014; Zhou et al. 2011; Ang & Gillis 2019) consists of the following two subproblems,

- QP(A): optimization of a quadratic form for \mathbf{a}_k (the column vector of A)
- QP(X): optimization of a quadratic form for \mathbf{x}_k (the row vector of X)

The block coordinate descent solves these quadratic problems (QP(A) and QP(X)) iteratively using a non-negative least square (NNLS) scheme. In this appendix, we derive the quadratic forms and then explain the projected gradient descent and its accelerated versions as the NNLS solver.

B.1. Quadratic Programming

QUADRATIC FORM FOR \mathbf{a}_k

A (log) likelihood term for the weighted NMF is rewritten in the quadratic form,

$$\frac{1}{2} \|D - WAX\|_F^2 = \frac{1}{2} \sum_i \sum_l \left(\Delta_{il} - \sum_j W_{ij} A_{jk} X_{kl} \right)^2 \quad (\text{B18})$$

$$= \frac{1}{2} \sum_i \sum_l X_{kl} X_{lk}^T \left(\sum_j W_{ij} A_{jk} \right)^2 - \sum_i \sum_l \Delta_{li}^T \sum_j W_{ij} A_{jk} X_{kl} + \frac{1}{2} \|\Delta\|_F^2 \quad (\text{B19})$$

$$= \frac{1}{2} \sum_l X_{kl}^2 \sum_{j',j} A_{kj'}^T \left(\sum_i W_{j'i}^T W_{ij} \right) A_{jk} - \sum_j \left[\sum_l X_{kl} \left(\sum_i \Delta_{li}^T W_{ij} \right) \right] A_{jk} + \frac{1}{2} \|\Delta\|_F^2 \quad (\text{B20})$$

$$= \frac{1}{2} \mathbf{a}_k^T \mathcal{L}_A \mathbf{a}_k - \mathbf{l}_A^T \mathbf{a}_k + \text{const.} \quad (\text{B21})$$

where

$$\mathcal{L}_A \equiv \mathbf{x}_k^T \mathbf{x}_k W^T W \quad (\text{B22})$$

$$\mathbf{l}_A \equiv W^T \Delta \mathbf{x}_k, \quad (\text{B23})$$

and $\Delta = \Delta(k)$ is defined by $\Delta_{il} \equiv D_{il} - \sum_{s \neq k} \sum_j W_{ij} A_{js} X_{sl}$. The penalty of the Tikhonov regularization (L2 term) is

$$\frac{1}{2} \lambda_A \|A\|_F^2 = \frac{1}{2} \mathbf{a}_k^T \mathcal{T}_A \mathbf{a}_k + \text{const.} \quad (\text{B24})$$

$$\mathcal{T}_A \equiv \lambda_A I \quad (\text{B25})$$

Thus, the quadratic programming for the weighted NMF with a spatial Tikhonov regularization minimizes

$$q_A = \frac{1}{2} \mathbf{a}_k^T (\mathcal{L}_A + \mathcal{T}_A) \mathbf{a}_k - \mathbf{l}_A^T \mathbf{a}_k. \quad (\text{B26})$$

Table 1. Terms in quadratic problems.

term	cost function ($\times 2$)	\mathcal{W}_A or \mathcal{W}_X	\mathbf{b}_A or \mathbf{b}_X
likelihood for \mathbf{a}_k	$\ D - WAX\ _F^2$	$\mathcal{L}_A = \mathbf{x}_k^T \mathbf{x}_k W^T W$	$\mathbf{l}_A = W^T \Delta \mathbf{x}_k$
Tikhonov (L2) term for \mathbf{a}_k	$\lambda_A \ \mathbf{A}\ _F^2$	$\mathcal{T}_A = \lambda_A I_J$	-
likelihood for \mathbf{x}_k	$\ D - WAX\ _F^2$	$\mathcal{L}_X = \ W\mathbf{a}_k\ _2^2 I_L$	$\mathbf{l}_X = \Delta^T W \mathbf{a}_k$
Volume Regularization (Det)	$\lambda_X \det(X X^T)$	$\mathcal{D}_X = \lambda_X \det(\check{X}_k \check{X}_k^T) [I_L - \check{X}_k^T (\check{X}_k \check{X}_k^T)^{-1} \check{X}_k]$	-
Volume Regularization (Logdet)	$\lambda_X \log[\det(X X^T + \delta I_K)]$	$\mathcal{E}_X = \lambda_X \mu_{\min}^{-1} I_L$	-
Tikhonov (L2) term for \mathbf{x}_k	$\lambda_X \ \mathbf{X}\ _F^2$	$\mathcal{T}_X = \lambda_X I_L$	-

NOTE— \check{X}_k is a submatrix of X by removing the k -th row of X , $\Delta_{il} = D_{il} - \sum_{s \neq k} \sum_j W_{ij} A_{js} X_{sl}$, I_J (or I_L , I_K) is an identity matrix $\in \mathbb{R}^{N_j \times N_j}$ (or $\mathbb{R}^{N_l \times N_l}$, $\mathbb{R}^{N_k \times N_k}$), and δ is a small number (we adopt 10^{-6}). The minimum eigenvalue of $E = \det(X X^T + \delta I_K)$ is denoted by μ_{\min} . In practice, we use X in the previous iteration to compute \mathcal{E}_X (Ang & Gillis 2018).

QUADRATIC FORM FOR \mathbf{x}_K

Likewise, we obtain the (log) likelihood term as a quadratic form of \mathbf{x}_k from equation (B20) as,

$$\frac{1}{2} \|D - WAX\|_F^2 = \frac{1}{2} \mathbf{x}_k^T \mathcal{L}_X \mathbf{x}_k - \mathbf{l}_X^T \mathbf{x}_k + \text{const.} \quad (\text{B27})$$

$$\mathcal{L}_X \equiv \|W\mathbf{a}_k\|_2^2 I \quad (\text{B28})$$

$$\mathbf{l}_X \equiv \Delta^T W \mathbf{a}_k \quad (\text{B29})$$

The volume regularization of the Gram determinant term can be written in quadratic form of \mathbf{x}_k

$$\frac{1}{2} \lambda_X \det(X X^T) = \frac{1}{2} \mathbf{x}_k^T \mathcal{D}_X \mathbf{x}_k \quad (\text{B30})$$

$$\mathcal{D}_X \equiv \lambda_X \det(\check{X}_k \check{X}_k^T) \left[I - \check{X}_k^T (\check{X}_k \check{X}_k^T)^{-1} \check{X}_k \right], \quad (\text{B31})$$

where \check{X}_k is a submatrix of X when we remove the k -th row of X . The derivation of equation (B30) is given in Zhou et al. (2011).

In Table 1, we summarize the quadratic terms for different regularization types. This list also includes the log-determinant type of the volume regularization Ang & Gillis (2018) and a simple L2 term for \mathbf{x}_k .

B.2. Projected Gradient Descent

The projected gradient descent (PG) based methods to solve a quadratic problem,

$$\mathbf{q} = \mathbf{x}^T \mathcal{W} \mathbf{x} - \mathbf{b}^T \mathbf{x}. \quad (\text{B32})$$

is described. The gradient descent with a non-negative condition is given by

$$\mathbf{x}^{(t+1)} = \mathcal{P}[\mathbf{x}^{(t)} - \eta \nabla q] = \mathcal{P}[\mathbf{x}^{(t)} - \eta(\mathcal{W} \mathbf{x}^{(t)} - \mathbf{b})], \quad (\text{B33})$$

where the projection operator unto a non-negative orthant is defined by $\mathcal{P}[\mathbf{x}] = \{\max(x_k, 0)\}$. We obtain the PG algorithm by adopting the inverse of the Lipschitz constant L to η . As the Lipschitz constant, one can use the 2-norm of $\|\mathcal{W}\|_2 = \max(\|\mathcal{W}\mathbf{x}\|_2 / \|\mathbf{x}\|_2)$ for $\mathbf{x} \in \mathbb{R}^m, \mathbf{x} \neq 0$ or a Frobenius norm of $\|\mathcal{W}\|_F = \sqrt{\sum_j \sum_i \mathcal{W}_{ij}^2} = \sqrt{\text{tr}(\mathcal{W}^T \mathcal{W})}$. Although the 2-norm is more efficient than the Frobenius norm (i.e. $\|\mathcal{W}\|_F \geq \|\mathcal{W}\|_2$), the computational cost of the 2-norm is much higher than that of the Frobenius norm, especially for a large matrix⁶.

Projected Gradient Descent (PG)

Minimization of $q = \mathbf{x}^T \mathcal{W} \mathbf{x} - \mathbf{b}^T \mathbf{x}$

Initialization: $T = I - \mathcal{W}/L, \mathbf{s} = \mathbf{b}/L, \mathbf{x}_0$

⁶ Therefore, we use a 2-norm for X and a Frobenius norm for A .


```

while Condition do
   $\mathbf{x}^{(t+1)} = \mathcal{P}[T\mathbf{x}^{(t)} + \mathbf{s}]$ 
end while

```

The convergence rate of the PG algorithm is relatively slow. The PG algorithm with Nesterov's acceleration (Nesterov 1983) is called the accelerated projected gradient descent. The APG algorithm is summarized as follows.

Accelerated Projected Gradient Descent (APG)

Minimization of $q = \mathbf{x}^T \mathcal{W} \mathbf{x} - \mathbf{b}^T \mathbf{x}$

Initialization: $T = I - \mathcal{W}/L$, $\mathbf{s} = \mathbf{b}/L$, $\mathbf{x}^{(0)}, \mathbf{y}^{(0)} = \mathbf{x}^{(0)}$, $\alpha_0 = 0.9$

```

while Condition do
   $\mathbf{x}^{(t+1)} = \mathcal{P}[T\mathbf{y}^{(t)} + \mathbf{s}]$ 
   $\alpha_{t+1} = (\sqrt{\alpha_t^4 + 4\alpha_t^2} - \alpha_t^2)/2$ 
   $\beta_{t+1} = \alpha_t(1 - \alpha_t)/(\alpha_{t+1} + \alpha_t^2)$ 
   $\mathbf{y}^{(t+1)} = \mathbf{x}^{(t+1)} + \beta_{t+1}(\mathbf{x}^{(t+1)} - \mathbf{x}^{(t)})$ 
end while

```

A residual curve as a function of iteration using Nesterov's acceleration is not monotonic. Restarting Nesterov's acceleration when the residual increases significantly improves the convergence rate (Odonoghue & Candes 2015).

APG+restart

Minimization of $q = \mathbf{x}^T \mathcal{W} \mathbf{x} - \mathbf{b}^T \mathbf{x}$

Initialization: $T = I - \mathcal{W}/L$, $\mathbf{s} = \mathbf{b}/L$, $\mathbf{x}^{(0)}, \mathbf{y}^{(0)} = \mathbf{x}^{(0)}$, $\alpha_0 = 0.9$

```

while Condition do
   $\mathbf{x}^{(t+1)} = \mathcal{P}[T\mathbf{y}^{(t)} + \mathbf{s}]$ 
   $q^{(t+1)} = (\mathbf{x}^{(t+1)})^T \mathcal{W} \mathbf{x}^{(t+1)} - \mathbf{b}^T \mathbf{x}^{(t+1)}$ 
   $\alpha_{t+1} = (\sqrt{\alpha_t^4 + 4\alpha_t^2} - \alpha_t^2)/2$ 
   $\beta_{t+1} = \alpha_t(1 - \alpha_t)/(\alpha_{t+1} + \alpha_t^2)$ 
   $\mathbf{y}^{(t+1)} = \mathbf{x}^{(t+1)} + \beta_{t+1}(\mathbf{x}^{(t+1)} - \mathbf{x}^{(t)})$ 
  if  $q^{(t+1)} > q^{(t)}$  then
     $\mathbf{x}^{(t+1)} = \mathcal{P}[T\mathbf{x}^{(t)} + \mathbf{s}]$ 
     $\mathbf{y}^{(t+1)} = \mathbf{x}^{(t+1)}$ ,  $\alpha_{t+1} = \alpha_0$ 
  end if
end while

```

Figure 14 shows a comparison of the above three algorithm for a randomly generated matrix A and a vector \mathbf{p} as a quadratic problem ($\mathbf{x}^T \mathcal{W} \mathbf{x} - \mathbf{b}^T \mathbf{x}$) for $\mathcal{W} = A^T A$ (100×100 matrix) and $\mathbf{b} = A^T \mathbf{p}$. The residual after the t -th iteration is defined by $\|A\mathbf{x}^{(t)} - \mathbf{b}\|_2^2$, where $\mathbf{x}^{(t)}$ is the estimated value after t iterations.

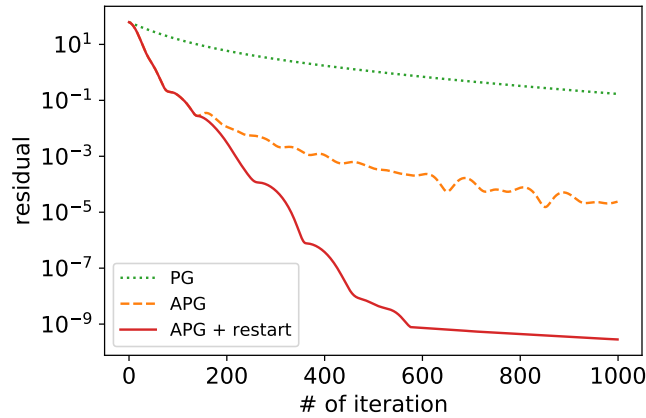


Figure 14. Residual of various PG solvers as a function of the number of iterations.

The drawback of the PG and APG method is that convergence is sensitive to the initial point. When all the components of $\mathcal{P}[\mathbf{x}^0 - \eta\Delta Q]$ are zero, the algorithm fails.

C. OPTIMIZATION OF WEIGHTED NMF BY MULTIPLICATIVE UPDATE

The multiplicative iterative algorithm (Lee & Seung 2001) is often used to minimize the cost function of the standard NMF, given in equation (17). It can be directly derived from the cost function and the Karush–Kuhn–Tucker first-order optimal conditions (Cichocki et al. 2009). We need to extend the standard multiplicative iterative algorithm to include the geometric kernel W in equation (27).

First, Let us explain the algorithm for the weighted NMF with no regularization term ($R(A) = 0$). Following the derivation of the multiplicative iterative algorithm, we compute the derivative of the cost function (27) as

$$\nabla_A Q = W^T W A X X^T - W^T D X^T \quad (\text{C34})$$

$$\nabla_X Q = A^T W^T W A X - A^T W^T D. \quad (\text{C35})$$

To ensure the nonnegativity, we divide the derivative of the cost function into the positive terms and negative terms

$$\nabla Q = [\nabla Q]_+ - [\nabla Q]_- = 0, \quad (\text{C36})$$

where $[\nabla Q]_- \geq 0, [\nabla Q]_+ \geq 0$. The multiplicative update is an operation that multiplies $[\nabla Q]_- / [\nabla Q]_+$ by A or X . This procedure can be interpreted as the steepest gradient descent

$$A \leftarrow A - \eta_A \odot \nabla_A Q \quad (\text{C37})$$

$$\eta_A = A \oslash [\nabla_A Q]_+ \quad (\text{C38})$$

and

$$X \leftarrow X - \eta_X \odot \nabla_X Q \quad (\text{C39})$$

$$\eta_X = X \oslash [\nabla_X Q]_+ \quad (\text{C40})$$

where \odot indicates the Hadamard product (the element-wise product of two matrices) and \oslash is the element-wise division.

The multiplicative iterative algorithm for the weighted NMF with no regularization is given by

$$A_{jk} \leftarrow A_{jk} \frac{[W^T D X^T]_{jk} + \epsilon}{[W^T W A X X^T]_{jk} + \epsilon} \quad (\text{C41})$$

$$X_{kl} \leftarrow X_{kl} \frac{[A^T W^T D]_{kl} + \epsilon}{[A^T W^T W A X]_{kl} + \epsilon}, \quad (\text{C42})$$

where ϵ is a small value to prevent division by zero. To include the regularization, the derivative of $R(A, X)$ by A or X is needed. For the dual-L2 type, we obtain

$$\nabla_A R(A, X) = \lambda_A A \quad (\text{C43})$$

$$\nabla_X R(A, X) = \lambda_X X. \quad (\text{C44})$$

Because these values remain positive when we take positive values for the initial state, the multiplicative update for the dual L2-type regularization is expressed as

$$\text{U(A): } A_{jk} \leftarrow A_{jk} \frac{[W^T D X^T]_{jk} + \epsilon}{[W^T W A X X^T + \lambda_A A]_{jk} + \epsilon} \quad (\text{C45})$$

$$\text{U(X): } X_{kl} \leftarrow X_{kl} \frac{[A^T W^T D]_{kl} + \epsilon}{[A^T W^T W A X + \lambda_X X]_{kl} + \epsilon}. \quad (\text{C46})$$

D. ON THE ADDITIONAL CONSTRAINTS

In remote sensing, an additional constraint is sometimes applied. For instance, the normalization for a spectrum is expressed by

$$\sum_l X_{kl} = 1. \quad (\text{D47})$$

We found that the constraint of (D47) functions as a form of regularization if we combine the constraint with the volume regularization term. When we use the constraint of (D47) with the volume-regularization term, the effect of the volume-regularization vanishes. We do not recommend that the constraint of (D47) is used in our case.

REFERENCES

- Aizawa, M., Kawahara, H., & Fan, S. 2020, under review
- Ang, M. A., & Gillis, N. 2018, in 2018 9th Workshop on Hyperspectral Image and Signal Processing: Evolution in Remote Sensing (WHISPERS), IEEE, 1–5
- Ang, M. S., & Gillis, N. 2019, arXiv e-prints, arXiv:1903.04362. <https://arxiv.org/abs/1903.04362>
- Baldrige, A. M., Hook, S., Grove, C., & Rivera, G. 2009, Remote Sensing of Environment, 113, 711
- Berdugina, S. V., & Kuhn, J. R. 2019, AJ, 158, 246, doi: [10.3847/1538-3881/ab2df3](https://doi.org/10.3847/1538-3881/ab2df3)
- Cichocki, A., Zdunek, R., Phan, A. H., & Amari, S.-i. 2009, Nonnegative matrix and tensor factorizations: applications to exploratory multi-way data analysis and blind source separation (John Wiley & Sons)
- Cowan, N. B., Fuentes, P. A., & Haggard, H. M. 2013, MNRAS, 434, 2465, doi: [10.1093/mnras/stt1191](https://doi.org/10.1093/mnras/stt1191)
- Cowan, N. B., & Strait, T. E. 2013, ApJL, 765, L17, doi: [10.1088/2041-8205/765/1/L17](https://doi.org/10.1088/2041-8205/765/1/L17)
- Cowan, N. B., Agol, E., Meadows, V. S., et al. 2009, ApJ, 700, 915, doi: [10.1088/0004-637X/700/2/915](https://doi.org/10.1088/0004-637X/700/2/915)
- Craig, M. D. 1994, IEEE Transactions on Geoscience and Remote Sensing, 32, 542, doi: [10.1109/36.297973](https://doi.org/10.1109/36.297973)
- Fan, S., Li, C., Li, J.-Z., et al. 2019, ApJL, 882, L1, doi: [10.3847/2041-8213/ab3a49](https://doi.org/10.3847/2041-8213/ab3a49)
- Farr, B., Farr, W. M., Cowan, N. B., Haggard, H. M., & Robinson, T. 2018, AJ, 156, 146, doi: [10.3847/1538-3881/aad775](https://doi.org/10.3847/1538-3881/aad775)
- Ford, E. B., Seager, S., & Turner, E. L. 2001, Nature, 412, 885, doi: [10.1038/35091009](https://doi.org/10.1038/35091009)
- Fu, X., Huang, K., Sidiropoulos, N. D., & Ma, W.-K. 2019, IEEE Signal Processing Magazine, 36, 59, doi: [10.1109/MSP.2018.2877582](https://doi.org/10.1109/MSP.2018.2877582)
- Fu, X., Ma, W.-K., Huang, K., & Sidiropoulos, N. D. 2015, IEEE Transactions on Signal Processing, 63, 2306, doi: [10.1109/TSP.2015.2404577](https://doi.org/10.1109/TSP.2015.2404577)
- Fujii, Y., & Kawahara, H. 2012, ApJ, 755, 101, doi: [10.1088/0004-637X/755/2/101](https://doi.org/10.1088/0004-637X/755/2/101)
- Fujii, Y., Kawahara, H., Suto, Y., et al. 2011, ApJ, 738, 184, doi: [10.1088/0004-637X/738/2/184](https://doi.org/10.1088/0004-637X/738/2/184)
- . 2010, ApJ, 715, 866, doi: [10.1088/0004-637X/715/2/866](https://doi.org/10.1088/0004-637X/715/2/866)
- Fujii, Y., Lustig-Yaeger, J., & Cowan, N. B. 2017, AJ, 154, 189, doi: [10.3847/1538-3881/aa89f1](https://doi.org/10.3847/1538-3881/aa89f1)
- Górski, K. M., Hivon, E., Banday, A. J., et al. 2005, ApJ, 622, 759, doi: [10.1086/427976](https://doi.org/10.1086/427976)
- Haggard, H. M., & Cowan, N. B. 2018, MNRAS, 478, 371, doi: [10.1093/mnras/sty1019](https://doi.org/10.1093/mnras/sty1019)
- Jiang, J. H., Zhai, A. J., Herman, J., et al. 2018, AJ, 156, 26, doi: [10.3847/1538-3881/aac6e2](https://doi.org/10.3847/1538-3881/aac6e2)
- Kawahara, H. 2016, ApJ, 822, 112, doi: [10.3847/0004-637X/822/2/112](https://doi.org/10.3847/0004-637X/822/2/112)
- Kawahara, H., & Fujii, Y. 2010, ApJ, 720, 1333, doi: [10.1088/0004-637X/720/2/1333](https://doi.org/10.1088/0004-637X/720/2/1333)
- . 2011, ApJL, 739, L62, doi: [10.1088/2041-8205/739/2/L62](https://doi.org/10.1088/2041-8205/739/2/L62)
- Kim, J., He, Y., & Park, H. 2014, Journal of Global Optimization, 58, 285
- Lawson, C. L., & Hanson, R. J. 1995, Solving least squares problems, Vol. 15 (Siam)
- Lee, D. D., & Seung, H. S. 2001, in Advances in neural information processing systems, 556–562
- Lin, C.-H., Ma, W.-K., Li, W.-C., Chi, C.-Y., & Ambikapathi, A. 2015, IEEE Transactions on Geoscience and Remote Sensing, 53, 5530, doi: [10.1109/TGRS.2015.2424719](https://doi.org/10.1109/TGRS.2015.2424719)
- Lin, C.-H., Ma, W.-K., Li, W.-C., Chi, C.-Y., & Ambikapathi, A. 2015, IEEE Transactions on Geoscience and Remote Sensing, 53, 5530
- Luger, R., Bedell, M., Vanderspek, R., & Burke, C. J. 2019, arXiv e-prints, arXiv:1903.12182. <https://arxiv.org/abs/1903.12182>
- Lustig-Yaeger, J., Meadows, V. S., Tovar Mendoza, G., et al. 2018, AJ, 156, 301, doi: [10.3847/1538-3881/aaed3a](https://doi.org/10.3847/1538-3881/aaed3a)
- McLinden, C. A., McConnell, J. C., Griffioen, E., McElroy, C. T., & Pfister, L. 1997, J. Geophys. Res., 102, 18,801, doi: [10.1029/97JD01079](https://doi.org/10.1029/97JD01079)

- Nakagawa, Y., Kodama, T., & Ishiwatari, M. 2020, under review
- Nesterov, Y. E. 1983, in Dokl. akad. nauk Sssr, Vol. 269, 543–547
- Oakley, P. H. H., & Cash, W. 2009, ApJ, 700, 1428, doi: [10.1088/0004-637X/700/2/1428](https://doi.org/10.1088/0004-637X/700/2/1428)
- Odonoghue, B., & Candes, E. 2015, Foundations of computational mathematics, 15, 715
- Paatero, P., & Tapper, U. 1994, Environmetrics, 5, 111
- Pallé, E., Ford, E. B., Seager, S., Montañés-Rodríguez, P., & Vazquez, M. 2008, ApJ, 676, 1319, doi: [10.1086/528677](https://doi.org/10.1086/528677)
- Schachtner, R., Pöppel, G., Tomé, A. M., & Lang, E. W. 2009, in International Conference on Independent Component Analysis and Signal Separation, Springer, 106–113
- Schwartz, J. C., Sekowski, C., Haggard, H. M., Pallé, E., & Cowan, N. B. 2016, MNRAS, 457, 926, doi: [10.1093/mnras/stw068](https://doi.org/10.1093/mnras/stw068)
- Vavasis, S. A. 2009, SIAM Journal on Optimization, 20, 1364
- Xiang, Y., Peng, D., & Yang, Z. 2015, Blind source separation: dependent component analysis (Springer)
- Zhou, G., Xie, S., Yang, Z., Yang, J.-M., & He, Z. 2011, IEEE transactions on neural networks, 22, 1626